lubricants

Article

A Study on the Thermal Properties of Oil-Film Viscosity in Squeeze Film Dampers

Hailun Zhou [1,*], Gangyi Cao [1], Xi Chen [2], Yuqi Zhang [1] and Yangguang Cang [1]

[1] School of Aeroengine, Shenyang Aerospace University, Shenyang 110136, China
[2] Wuxi Orient Software Technology Co., Ltd., Wuxi 214082, China
[*] Correspondence: hlzhou@sau.edu.cn

Abstract: Considering the variation in temperature of the oil film in squeeze film dampers (SFDs) caused by squeezing, a more comprehensive analysis of SFD can be obtained. Aiming to investigate the viscosity thermal effect of the oil film in SFDs, this study established a 3D CFD solution model. Based on the total energy model, the viscosity thermal effect was performed. With the mixture multi–phase flow model, the Zwart–Gerber–Belamri (Z–G–B) cavitation model, and the use of the additional mass coefficient, the two–phase flow phenomenon in SFDs was discussed. The oil film at various temperatures and the temperature distribution of different oil types under different working conditions were analyzed. Furthermore, the influence of the SFD thermal effect on the two–phase flow phenomenon were particularly carried out. Meanwhile, the simulation results of the SFD thermal effect were experimentally verified. The results revealed that the maximum temperature of the SFD oil film was enhanced with the increase in the eccentricity ratio and precession frequency. The temperature of the oil film was closely related to the oil dynamic viscosity. The dynamic viscosity of the oil was reduced, which was caused by the SFD thermal effect, thus leading to decreased oil–film damping, enlarging the vaporization level and the range of vapor cavitation, as well as the ingested air amount. CFD simulation results of the thermal effect were in good agreement with the experimental data, which verified the accuracy of the proposed model.

Keywords: squeeze film damper; thermal effect; two–phase flow; CFD

check for updates

Citation: Zhou, H.; Cao, G.; Chen, X.; Zhang, Y.; Cang, Y. A Study on the Thermal Properties of Oil-Film Viscosity in Squeeze Film Dampers. *Lubricants* **2023**, *11*, 163. https://doi.org/10.3390/lubricants11040163

Received: 5 March 2023
Revised: 24 March 2023
Accepted: 28 March 2023
Published: 1 April 2023

Correction Statement: This article has been republished with a minor change. The change does not affect the scientific content of the article and further details are available within the backmatter of the website version of this article.

1. Introduction

Squeeze film damper (SFD) is considered a very promising damping device, which is widely applied in high–speed rotating machinery, such as an aero–engines. As an effective and reliable vibration damper device, it has a simple structure and a very excellent damping effect due to its capacity to effectively reduce the vibration amplitude of the rotor and refrain from the instability of the system [1,2]. As we know, SFDs work by providing viscosity damping to absorb vibration energy. Oil viscosity is one of the major factors that decide the vibration damping performance. While viscosity is a function of the temperature, oil viscosity is affected by oil temperature. Because the oil film can be squeezed by the external force from the rotor system, the oil–film temperature may be greatly increased under the conditions of the large amplitude and high rotation speed of SFDs. Meanwhile, the two–phase flow phenomenon occurs in the actual working conditions of SFDs [3], which also act on the damping properties of SFDs.

At present, many researchers have studied factors such as the SFD thermal effect and two–phase flow. In terms of thermal effect, Perreault et al. [4] established a thermal hydrodynamic model (THD) of an SFD and studied the variation in the temperature field of the fluid in different working conditions and structures. Hamzehlouia and Behdinan [5] carried out thermal hydrodynamic analysis of an SFD by solving a numerical model, in which the temperature field of the journal and bush of the SFD were achieved by the Laplace heat conduction model. The results indicated that the thermal effect has significant influences on oil–film force. The maximum temperature of the oil film was enhanced with an increase in rotate speed and amplitude vibration. San Andrés and Diaz [6] investigated the oil–film temperature inside an SFD with a thermocouple under the help of the rotor device. The results showed that in the case of large eccentricity, the oil–film temperature of the sensing point can be up to 10 °C higher than the entrance. Furthermore, San Andrés et al. [7] established a model of floating bearing, in which the coupling heat transfer was considered and the thermal hydrodynamic was analyzed. Yang et al. [8] proposed a high–flow thermohydrodynamic model for the prediction of turbulence and dynamic characteristics. Regarding the two–phase flow aspect, Troy et al. [9] proposed a physical state cavitation model and solved the Rayleigh–Plesset and Reynolds equations in a transient environment. Tao et al. [10] established an SFD model considering oil and air mixing in isothermal conditions. The peak pressure and force of the oil film were analyzed. Zhou et al. [11] used a multi–phase flow CFD model, which considered air ingestion. The numerical simulation results were verified by bidirectional incentive experiments. The results showed that oil–film damping in different working conditions is consistent with the experimental results. However, with the increase in eccentricity, the difference between CFD results and experimental oil–film damping gradually increased. The reason for this could be summarized without considering the SFD thermal effect during the simulation. Gehannin and Arghir et al. [12] calculated vapor cavitation and air ingestion by solving the Rayleigh–Plesset equation and the volume of fluid (VOF) method, respectively. They found that vapor cavitation was mostly located in low–pressure zones, and vapor pressure was approaching absolute zero pressure. Alternately, air ingestion had a constant pressure zone, and the pressure was very close to the atmospheric pressure. Meanwhile, the accuracy of the numerical simulation was verified in virtue of the experimental data of oil pressure from Adiletta and Pietra [13]. Bonello [14] found that vapor cavitation reduces excessive rotor vibration to some extent, so it is not appropriate to increase the oil supply pressure to eliminate vapor cavitation when static eccentricity or unbalance is large. Fan et al. [15] analyzed the influence of fluid inertia on vapor cavitation using the Elrod algorithm and Gumbel cavitation boundary conditions and verified the accuracy of the model via experiment. San Andres et al. [6,16,17] conducted experiments on rotors installed with different SFDs and studied the influence of two–phase flow on the dynamic characteristics of SFDs by directly controlling the oil–film mixing ratio. In addition, bidirectional excitation test were conducted, the phenomenon of oil–film air ingestion under different speeds and different oil supply pressures was observed by high–speed cameras using the visualization test method. They also carried out related research on SFDs with a sealing device [18,19]. Bakir et al. [20] established an enhanced cavitation model and used the Rayleigh–Plesset equation as the basic equation reflecting the cavitation changes. Xing et al. [21] established a three–dimensional CFD homogeneous cavitation model based on the Navier-Stokes (NS) equation and analyzed the oil–film pressure distribution and gas density distribution. Milind [22] used CFD software Fluent to study the vapor cavitation in an SFD; however, the oil–film pressure results were slightly larger than the test results, possibly because the numerical simulation does not consider the existence of air ingestion.

From previous, works we found that the CFD study of two–phase flow in SFDs is not comprehensive, and there is little literature focusing on the thermal effects of SFD. It is necessary to reveal the performance of the thermal effects on two–phase flow phenomena. In addition, air ingestion and vapor cavitation occur simultaneously. However, current research tends to explore them separately, before testing or simulating them individually. In order to study the SFD thermal effect and two–phase flow more extensively, a CFD model considering SFD thermal effects and two–phase flow is established. By analyzing the calculation results, the mutual influence rule among the thermal effect, air ingestion, vapor cavitation, and damping characteristics are clearly revealed.

In view of the above aspects, the dynamic characteristics of the squeeze film damper are discovered in the present study by the methods of theoretical analysis, numerical simulation, and experiment. Firstly, based on the analysis of the governing equation of two–phase flow, an SFD thermohydrodynamic model is established, and detailed thermohydrodynamic analysis is developed. Secondly, the influences of viscosity thermal effect on SFD dynamic performance and oil–film temperature are studied. The variation law of two–phase flow with the viscosity thermal effect is revealed. Finally, the accuracy of SFD thermal–effect calculations is verified by comparing the experimental results.

2. CFD Numerical Solution

The governing equation of numerical solution for the viscosity thermal effect of the oil film includes the continuity equation, momentum equation, and energy equation. Meanwhile, the SFD fluid domain should also take consideration of the two–phase flow. The total energy model should be used to solve the SFD thermal effect because this model contains a working term and involves consideration for the thermal change caused by the fluid kinetic energy. As for the two–phase flow solution, the mixture homogeneous phase model is used to solve the homogeneous phase 3D Navier–Stokes (N–S) equation to obtain the pressure field of the fluid domain. The continuity equation of the homogeneous phase is shown as follows:

$$\frac{\partial}{\partial t}(r_\alpha \rho_\alpha) + \nabla(r_\alpha \rho_\alpha U_\alpha) = 0 \tag{1}$$

The homogeneous phase momentum equation is shown as follows:

$$\frac{\partial}{\partial t}(\rho U) + \nabla\cdot\left(\rho U\cdot U - \mu\left(\nabla U + (\nabla U)^T\right)\right) = S_M - \nabla p \tag{2}$$

With the influence of the viscosity thermal effect of the oil, the energy equation of the multi–phase flow model is shown as follows:

$$\frac{\partial(\rho h_{tot})}{\partial t} - \frac{\partial \rho}{\partial t} + \nabla\cdot(\rho U_{tot}) = \nabla\cdot(\lambda \nabla T) + \nabla\cdot(U\cdot\tau) + U\cdot S_M + S_E \tag{3}$$

As can be seen in the equation, r_α is the volume fraction of each phase, $\sum r_\alpha = 1$ is the sum of volume fraction, N_p is the number of phases, $1 \leq \alpha \leq N_p$; ρ_α is the density of each phase, and $\rho = \sum r_\alpha \rho_\alpha$; U_α is the velocity vector of each phase. A homogeneous phase model assumes that the velocity vector of each phase is equal in momentum transfer, namely $U_\alpha = U$. For $\mu = \sum r_\alpha \mu_\alpha$, μ_α is the dynamic viscosity of each phase and p is the pressure. S_M is the term of generalized momentum source. h_{tot} is total enthalpy, $h_{tot} = h + 1/2U^2$; $\nabla \cdot (U \cdot \tau)$ is defined as the working coefficient of the viscous stress.

By solving the 3D N–S equation, we obtain oil–film pressure P. Then, we have the tangential force of the oil film, F_t.

$$F_t = \int_0^L \int_0^{2\pi} p(\theta)\sin\,\theta r_b\, d\theta\, dZ \tag{4}$$

where L is the axial length of damper, p is the oil–film pressure, θ is the procession angle, and r_b is the radius of journal.

From Formula (5), we can obtain the equivalent oil–film damping of the SFD. In this formula, the minus represents that the tangential force is in the opposite direction to the motion.

$$C = -\frac{F_t}{e\Omega} \tag{5}$$

where e is the dynamic eccentric distance and Ω is the procession rotation speed.

On the basis of solving the two–phase flow control equation, and when both axial ends of the SFD are exposed to the external environment without end sealing, large amounts of air are sucked in, which means the external air is sucked into the damper. According to the setting of boundary conditions, it is required to add the air volume fraction as an additional mass coefficient. Therefore, we need to solve the transmission equation, including the additional mass coefficient of the air volume fraction as follows:

$$\frac{\partial}{\partial t}(\rho\phi) + \nabla \cdot (\rho U \phi) = \nabla \cdot \left(\rho D_{\varphi} \nabla \phi\right) + S_{\phi} \tag{6}$$

When the vapor cavitation in two–phase flow is considered, the transfer equation between two phases is shown as follows:

$$\frac{\partial}{\partial t}(r_{\alpha}\rho_{\alpha}) + \nabla(r_{\alpha}\rho_{\alpha}U_{\alpha}) = S_{\alpha} + \Gamma_{\alpha} \tag{7}$$

Here, S_{α} is a special mass source term determined by cavitation transfer, and Γ_{α} is the mass source in each phase due to the transfer of unit volume between phases.

Therefore, the transfer equation between phases can be expressed as:

$$\frac{\partial}{\partial t}(r_{\alpha}\rho_{\alpha}) + \nabla(r_{\alpha}\rho_{\alpha}U_{\alpha}) = R_{e} - R_{c} \tag{8}$$

Here, R_e is the mass source term of the vapor formed by evaporation, and R_c is the mass source term of the liquid caused by condensation. Grease evaporation and cavitation condensation happen simultaneously, which are determined by the pressure of the oil film.

The creation rate of vaporization and the condensation rate are obtained based on the Rayleigh–Plesset (RP) equation. The RP equation describes the essential process of vaporization and condensation. The Rayleigh–Plesset equation is shown as follows:

$$R_B \frac{d^2 R_B}{dt^2} + \frac{3}{2}\left(\frac{dR_B}{dt}\right)^2 + \frac{2\sigma}{\rho_f R_B} = \frac{p_v - p}{\rho_f} \tag{9}$$

In this formula, R_B represents the radius of bubbles, p_v is the saturated vapor pressure of liquid, p is the liquid pressure around the bubbles, ρ_f is the liquid density, and σ is the surface tension coefficient. It is assumed that the fluid exists under the condition of low oscillation frequency and the Reynolds number. Therefore, the second–order term and surface tension coefficient are neglected, and the RP equation can be simplified as follows:

$$\frac{dR_B}{dt} = \sqrt{\frac{2}{3}\frac{p_v - p}{p_f}} \tag{10}$$

This simplified Rayleigh–Plesset equation can serve as a mass source term in the deduction of any cavitation model. In the cavitation model of Zwart–Gerber–Belamri (Z–G–B) [23], assuming that bubbles do not interact with each other, the radius of the bubbles is consistent. The change rate of the bubble volume is shown as follows:

$$\frac{dV_B}{dt} = 4\pi {R_B}^2 \sqrt{\frac{2}{3}\frac{p_v - p}{p_f}} \tag{11}$$

The mass change rate is shown as:

$$\frac{dM_B}{dt} = 4\pi {R_B}^2 \rho_g \sqrt{\frac{2}{3}\frac{p_v - p}{p_f}} \tag{12}$$

Assuming that the number of bubbles per unit volume is N_B, air volume fraction r_g is expressed as:

$$r_g = V_B N_B = \frac{4}{3}\pi {R_B}^3 N_B \tag{13}$$

The total interphase transfer rate of mass per unit volume is shown as follows:

$$m_{fg} = N_B \frac{dM_B}{dt} = \frac{3r_g \rho_g}{R_B} \sqrt{\frac{2}{3} \frac{p_v - p}{p_f}} \tag{14}$$

The change per unit volume for bubble vaporization and condensation is shown in Equations (15) and (16), respectively. F is defined as the empirical coefficient, which represents the change rate of the bubble vaporization and condensation. In CFX, bubble radius RB is substituted for Rnuc, the one in the position where the bubble core is formed, without considering the influence of thermal hydrodynamic force:

When $p < p_v$, bubbles are created:

$$m^{+}{}_{fg} = F \frac{3r_{nuc}(1 - r_g)\rho_g}{R_{nuc}} \sqrt{\frac{2}{3} \frac{|p_v - p|}{\rho_f}} \operatorname{sgn}(p_v - p) \tag{15}$$

When $p > p_v$, bubbles are condensed:

$$m^{-}{}_{fg} = F \frac{3r_g \rho_g}{R_B} \sqrt{\frac{2}{3} \frac{|p_v - p|}{\rho_f}} \operatorname{sgn}(p_v - p) \tag{16}$$

In which bubble radius $R_{nuc} = 1$ µm, volume fraction in bubble core $r_{nuc} = 5 \times 10^{-4}$, bubble vaporization coefficient $F_{\text{vap}} = 50$, and bubble condensation coefficient $F_{\text{cond}} = 0.01$.

By solving the energy equation, this paper takes the viscosity enthalpy created by the SFD into consideration. As the temperature of the SFD varies according to the working conditions, enthalpy is the function of the temperature, namely $\Delta H(T)$. Therefore, the mass source term of the revised Z–G–B cavitation model [24,25] can be expressed as Equations (17) and (18). According to the aerodynamic theory, on the interface of gas and liquid, the molecule exchange potential between liquid and steam is inversely proportional to the square root of the temperature.

When $p < p_v(T)$, bubble vaporization is shown as:

$$S^{+} = m^{+}{}_{fg} \Delta H(T) = F_{\text{vap}} \frac{3r_{nuc}(1 - r_g)\rho_g}{\sqrt{T} R_{nuc}} \sqrt{\frac{2}{3} \frac{|p_v - p|}{\rho_f}} \operatorname{sgn}(p_v - p) \Delta H(T) \tag{17}$$

When $p > p_v(T)$, bubble condensation is shown as:

$$S^{-} = m^{-}{}_{fg} \Delta H(T) = F_{\text{cond}} \frac{3r_{nuc} r_g \rho_g}{\sqrt{T} R_{nuc}} \sqrt{\frac{2}{3} \frac{|p_v - p|}{\rho_f}} \operatorname{sgn}(p_v - p) \Delta H(T) \tag{18}$$

The saturated vapor pressure pv of cavitation follows the saturated vapor pressure of oil, i.e., −72,139.79 Pa [26], provided by the literature [26], with absolute pressure being 29,170.21 Pa. As the Reynolds number of the SFD is small, the flow condition is assumed to be laminar flow [27]. The reference pressure of the fluid domain is set as the atmosphere pressure.

3. SFD Thermal Effect Analysis

Firstly, to find out the influence of the thermal effect on the dynamic properties of the SFD, a study was carried out on the temperature–viscosity effect of SFD without considering the influence of two–phase flow. To obtain greater clarity on the influence of the temperature–viscosity effect on the temperature, oil damping, and temperature distribution of the oil film, we temporarily excluded the influence of oil supply conditions on the thermal effect. Secondly, based on a study on the oil viscosity thermal effect, a study was developed to investigate the influence of the thermal effect on vapor cavitation and air suction phenomenon.

3.1. Model and Meshing

Geometric dimensions of the model and oil parameters are listed in Table 1. The SFD fluid domain model is shown in Figure 1a, and the mesh generation is shown in Figure 1b. To be clear, the number of meshes in the figure is only 25% of the number in the numerical simulation. As the thickness of the oil film is very low, although it makes a great difference to the result of the calculation, mesh refinement in the thickness direction is required, which has been studied in detail in the literature [28]. To take into account the precision and calculation time, as well as the irrelevance verification of mesh, we finally confirmed the number of nodes, including 240 in the circumferential direction, 80 in the axial direction, and 10 in the radial direction. This means that the mesh has a circumferential dimension of 1mm, an axial dimension of 0.25 mm, and a radial dimension of 0.014 mm. According to statistics, the number of nodes is 212,058 and the number of meshes is 190,400.

Table 1. Geometric Dimensions and Oil Parameters.

Name	Symbol	Value	Dimension
Shaft diameter	D	73.8	mm
Clearance	c	0.14	mm
Axial length	L	20.6	mm
Thermal conductivity	K	0.13	W/m·K
Heat capacity	C	2000	J/kg·K

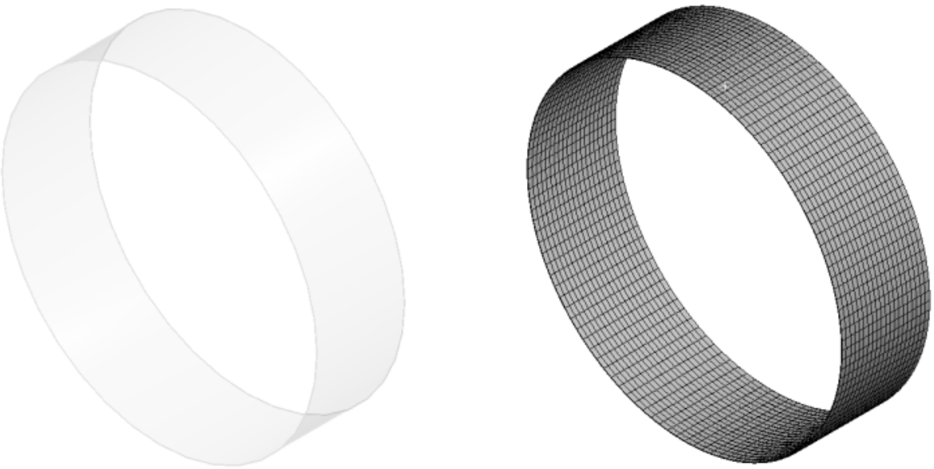
(**a**) (**b**)

Figure 1. SFD model: (**a**) SFD fluid domain model; (**b**) SFD mesh.

3.2. Boundary Conditions

The boundary conditions of the SFD with both axial open ends are shown in Figure 2, in which the journal and outer ring are set to be adiabatic "Wall" boundaries. The wall of the outer ring is fixed without slipping and the wall of the journal makes simulated procession. The motion equation is shown as follows:

$$\begin{cases} X = e\cos(\Omega t) \\ Y = e\sin(\Omega t) \end{cases} \tag{19}$$

In which t presents time. Different procession amplitudes and frequencies are simulated by varying dynamic eccentric distance e and procession rotation speed Ω. The relationship between procession rotation speed and frequency is $\Omega = 2\pi f$, $e/c = \varepsilon$, where ε represents the dimensionless eccentricity ratio. Both axial ends are set to be "opening", i.e., the free opening boundary where oil flows in and out. The reference temperature is 23 °C.

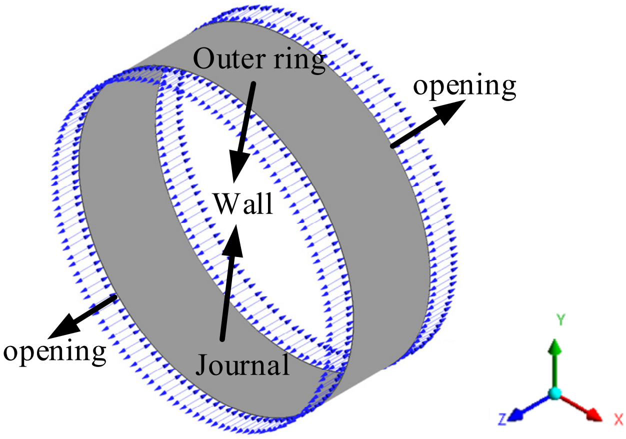

Figure 2. SFD boundary conditions.

3.3. The Analysis of SFD Thermal Effect

Squeezed by the external force from the rotor, the SFD absorbs vibration energy. Due to the function of the internal friction in the oil film, heat is generated and thus enhances the temperature of the oil film. The heat created by internal friction is related to the working condition of the SFD and the viscosity of the oil. Oil–film temperature varies with the type of oil and the working condition of the SFD. Oil viscosity is greatly reduced by the excessively high temperature of the oil film, which may result in the failure of the SFD.

Therefore, aiming to observe the oil–film temperature variation of different types of oil in different working conditions, we chose a high–viscosity oil ISO VG68 [6] and low–viscosity oil ISO VG2 [29] to provide a numerical simulation. The temperature–viscosity relationship of ISOVG68 and ISO VG2 is $\mu = 0.1565e^{(-0.057(T-22.4))}$ and $\mu = 0.00296e^{(-0.0187(T-25.2))}$, respectively, in which μ represents the dynamic viscosity of oil (the unit is Pa·s) and T represents the temperature (the unit is °C).

SFD models of two oil types were simulated by software CFX, and related parameters included an eccentricity ratio of 0.3 and 0.4, procession frequency f, 75 Hz~175 Hz, and a reference temperature of 23 °C. The dynamic viscosity of VG68 was 0.151 Pa·s and VG2 was 0.0031 Pa·s. The densities were 877 kg/m^3 and 785 kg/m^3, respectively. By numerical simulation, the maximum temperature change in the oil film of two types is shown in Figure 3.

It can be seen from Figure 3 that with the increase in the precession frequency and the eccentricity ratio, the maximal temperature of the oil film increases gradually. However, Figure 3a shows that low–viscosity oil ISO VG2 does not have a significant increment of the maximum temperature, which is about 2 °C. Meanwhile, Figure 3b shows a different picture of ISO VG68. As a high–viscosity oil, it shows a significant temperature increment, which can be up to approximately 10 °C, which is very similar to the experiment result of the paper by San Andrés [6]. According to the rotor experiment of San Andrés, the temperature in the middle section of the oil film of the SFD is around 10 °C higher than the temperature at the entry. The distinct difference in temperature change is mainly due to the difference in viscosity in the way that with a higher dynamic viscosity, the oil–film temperature is higher under the same working conditions.

The change in dynamic viscosity is shown in Figure 4. The change tendency of viscosity is opposite to that of the temperature. It can be seen from Figure 4a that with the increase in procession frequency and eccentricity ratio, oil viscosity tends to decrease. As a low–viscosity oil, ISO VG2 has a smaller variation range in terms of viscosity. A distinct decline in viscosity only occurs at 175Hz. As observed from Figure 4b, with the increase in the procession frequency and eccentricity ratio, the viscosity of ISO VG68, a high–viscosity oil, declines significantly.

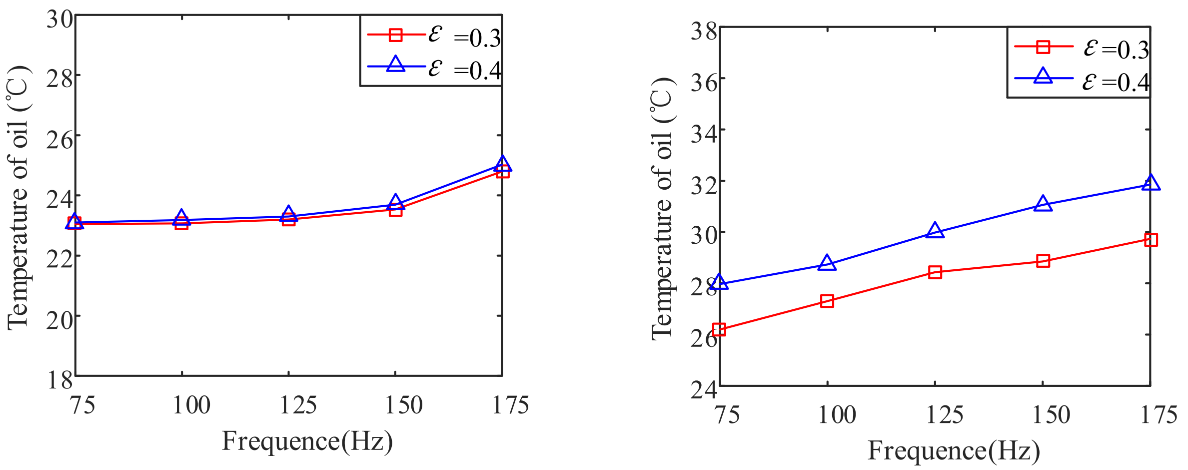

(**a**) (**b**)

Figure 3. Maximum temperature change curve of oil film: (**a**) Temperature change curve of VG2; (**b**) Temperature change curve of VG68.

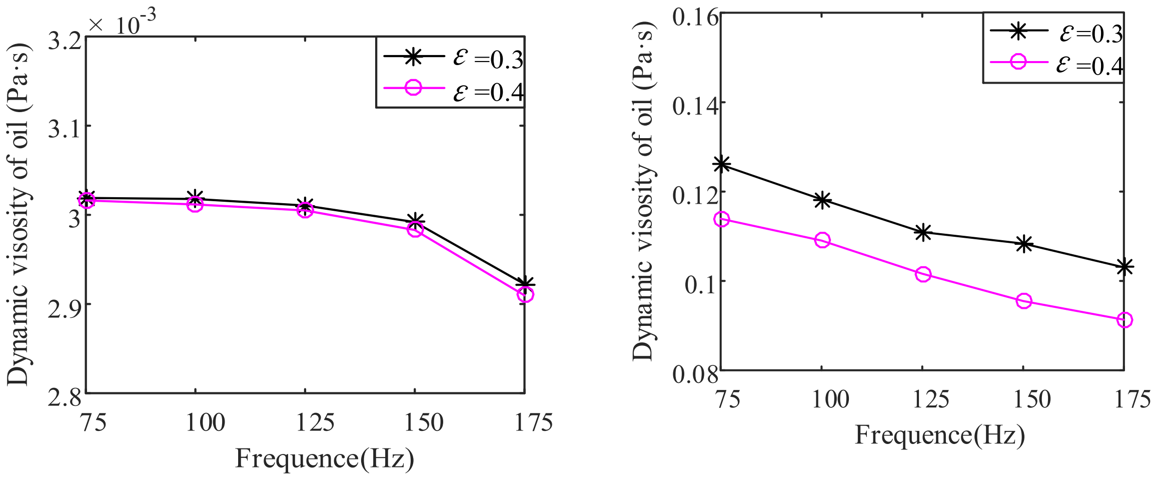

(**a**) (**b**)

Figure 4. Viscosity variation curve of different oil: (**a**) Viscosity variation curve of VG2; (**b**) Viscosity variation curve of VG68.

To develop the distribution of oil–film temperature, for example, where the eccentricity ratio ε is 0.4 and the procession frequency f is 125 Hz, the 3D plot of the temperature field and the oil–film pressure field is shown in Figure 5a. The oil–film temperature field of the SFD distributed in such a way that the temperature amid the oil film is the highest and decreases progressively from the axially (Z–axis) middle plane toward both ends, namely symmetric distribution surrounding the central plane.

Firstly, in order to clarify the distribution of oil–film temperature, according to the oil–film pressure distribution shown in Figure 5b, it should be noted that when the SFD performs a periodic circular motion, the high–pressure zone is located in the middle of the oil film. The oil–film pressure shows periodic variation. Therefore, the oil film in the center is under the greatest pressure. The shear force of viscosity functions and generates heat, raising the temperature of the oil film.

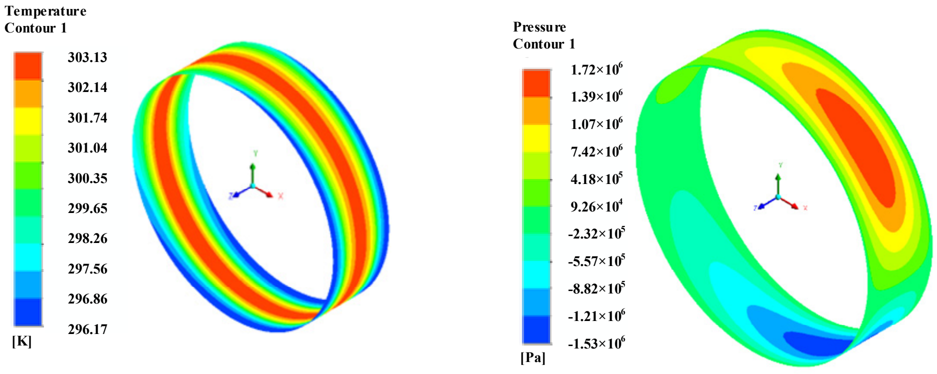

(**a**) (**b**)

Figure 5. Numerical simulation results: (**a**) Oil–film temperature field distribution.; (**b**) Oil–film pressure field distribution.

Secondly, as both axial ends of the SFD are opening boundaries, oil can be freely exchanged on both ends according to the pressure of the flow field and the environment. Therefore, low–temperature oil flows in from both ends and has a thermal transmission with high–temperature oil. However, the oil in the middle section cannot have a timely thermal transmission with the external environment.

For the above reasons, in the flow field of the SFD, oil–film temperature is in the gradient distribution in which the center is higher than both ends.

As the thermal effect raises the temperature of the oil film and reduces the dynamic viscosity of oil, the damping performance of the SFD is also weakened. With the thermal effect taken into consideration, the variation performance of oil–film damping is as shown in Figure 6. The oil–film damping of two types of oil increases with the increase in precession frequency when the eccentricity ratio is 0.3. When the SFD thermal effect is considered, oil–film damping is lower than that of the case without considering the thermal effect. The oil–film damping of ISO VG2 decreased by 1.4% at maximum, whereas that of ISO VG68 decreased by 15.9%.

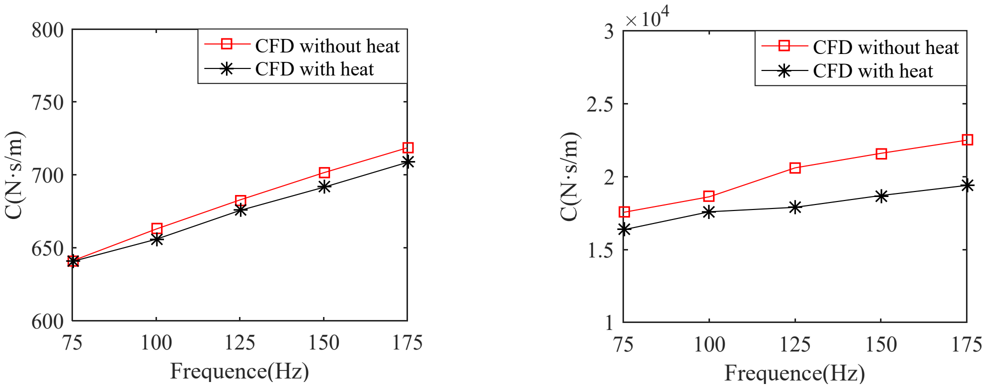

(**a**) (**b**)

Figure 6. The variation performance of oil–film damping: (**a**) Damping variation curve of VG2.; (**b**) Damping variation curve of VG68.

The main reason for this is that as the SFD thermal effect raises the temperature of the oil film resulting in the decrease in dynamic viscosity, oil–film damping declines. When the thermal effect is considered, the oil–film damping of ISO VG68 decreases more significantly, and with the increase in procession frequency f, the increment of oil–film damping tends to slow down, which proves that the temperature–viscosity effect of the high–viscosity oil is much more evident.

4. A Study on Two–Phase Flow Affected by Viscosity Thermal Effect

On the basis of the thermal effect study, we incorporated two–phase flow into consideration and studied the influence of the thermal effect on two–phase flow. The accuracy of numerical simulation with the thermal effect is verified by the experimental data. The two–phase flow phenomenon of the SFD includes cavitation the air ingestion. Cavitation mainly refers to vapor cavitation and air ingestion mainly occurs in the SFD with both ends open.

4.1. An Analysis on the Influence of Thermal Effect on Vapor Cavitation

As we know, while the SFD of aero–engines operates under high–temperature conditions, lower dynamic viscosity and excessive temperature variation also affect the saturated vapor pressure. It can be seen in Figure 3a that the increment of the oil–film temperature of ISO VG2 is not large. From that, low–viscosity oil ISO VG2 was chosen, and an SFD vapor cavitation model was created by numerical simulation under different eccentricity ratios ε and procession frequencies f, with thermal effect included. The absolute pressure variations in the oil film under different procession frequencies and eccentricity ratios in numerical simulation are shown in Figures 7 and 8, respectively. The oil–film pressure variations in Figures 7 and 8 present a similar variation rule. Based on the condition in which the eccentricity ratio is 0.4 and the peak pressure increases with the increase in procession frequency, the peak pressure plot is shown in Figure 7. When the procession frequency f is 100 Hz, the oil film maintains its state without vapor cavitation formed. The oil can resist some extent of low pressure before it reaches vaporization pressure. When procession frequency reaches 200 Hz and 300 Hz, the low pressure of the oil film achieves vaporization pressure, thus leading to vapor cavitation. It can be seen in Figure 8 that in the case of 200 Hz, with the increase in eccentricity ratio, the low–pressure oil film reaches saturated vapor pressure, resulting in vapor cavitation. This means with the increase in procession frequency and eccentricity ratio, oil vaporization occurs and forms vapor cavitation, and the vaporization pressure range gradually increases.

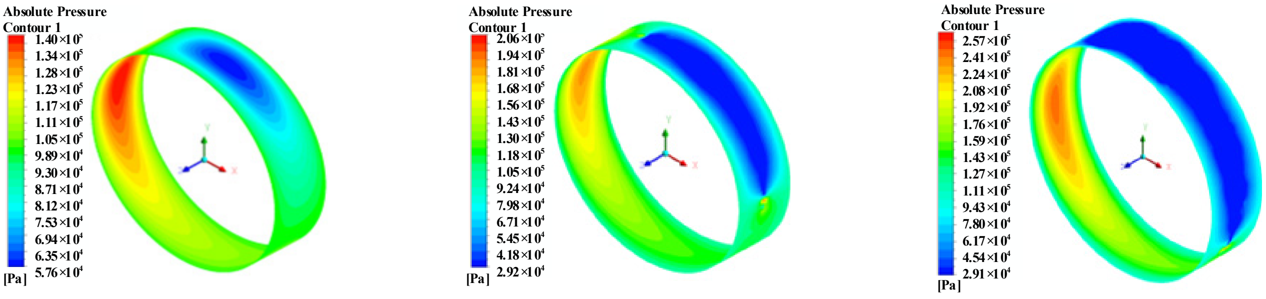

(**a**) (**b**) (**c**)

Figure 7. Oil–film absolute pressure with different procession frequencies f: (**a**) f = 100 Hz; (**b**) f = 200 Hz; (**c**) f = 300 Hz.

It is usually assumed in general analysis that a flow field has a constant temperature, so it is difficult to analyze the influence of the thermal effect on vapor cavitation. Without considering the thermal effect, vapor cavitation can be seen in Figure 9. With the increase in procession frequency and eccentricity ratio, the range of cavitation and vaporization degree gradually increases. This is due to the fact that with the increase in eccentricity ratio and procession frequency, the squeezing and divergence of the oil–film gap are both increased, thus resulting in lower negative pressure of the oil film and the enlargement of both the vapor cavitation degree and vaporization range.

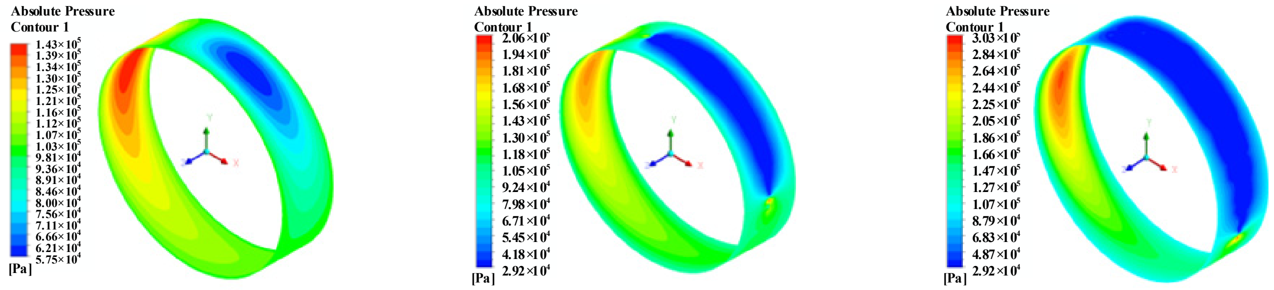

(**a**) (**b**) (**c**)

Figure 8. Oil–film absolute pressure with different eccentricity ratios ε: (**a**) ε = 0.3; (**b**) ε = 0.4; (**c**) ε = 0.5.

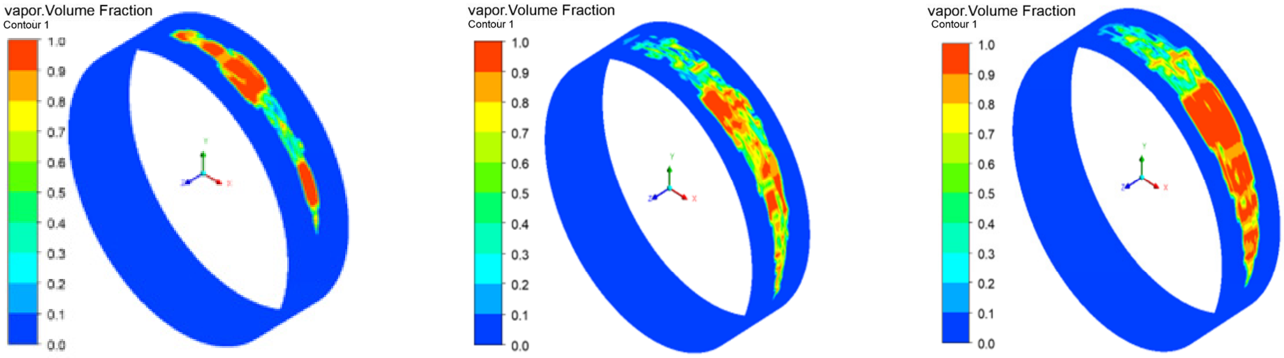

(**a**) (**b**) (**c**)

Figure 9. Cavitation without considering thermal effect: (**a**) ε = 0.4, f = 200 Hz; (**b**) ε = 0.4, f = 300 Hz; (**c**) ε = 0.5, f = 200 Hz.

As for vapor cavitation, it is not only associated with vaporized pressure; it is also affected by temperature. Vapor cavitation is a kind of vaporization when oil reaches the saturated pressure of the vapor; consequently, a two–phase flow of oil and vapor mixture is formed in the oil clearance of the SFD. Meanwhile, vaporization is also an endothermal process. It is generally discussed that saturated vapor pressure changes under high–temperature and high–pressure conditions but remains constant at room temperature. The thermal effect of the SFD refers to the viscosity thermal effect generated by squeezing the oil film. As known from Section 3, the temperature variation amplitude of oil ISO VG2 is very small.

According to the comparison between Figures 9 and 10, under the same working conditions, the vaporization of the case considering the thermal effect is much more evident than that without the case, and the cavitation range is larger. This is because oil vaporization is an endothermal process. While the viscosity heat of the oil film is considered, the oil is squeezed to generate the heat. However, part of the heat is transferred to the oil at the boundary of the axial ends according to the law of conservation of energy; however, most high–temperature oil is present in the central part of the SFD. According to Figures 9 and 10, the vapor cavitation generated in the low–pressure zone of the oil film is also located in the middle so that a great amount of heat generated by the oil is taken away by the vaporization of the cavitation from the leaving bubbles. Therefore, when the thermal effect is considered, vapor cavitation is much more obvious.

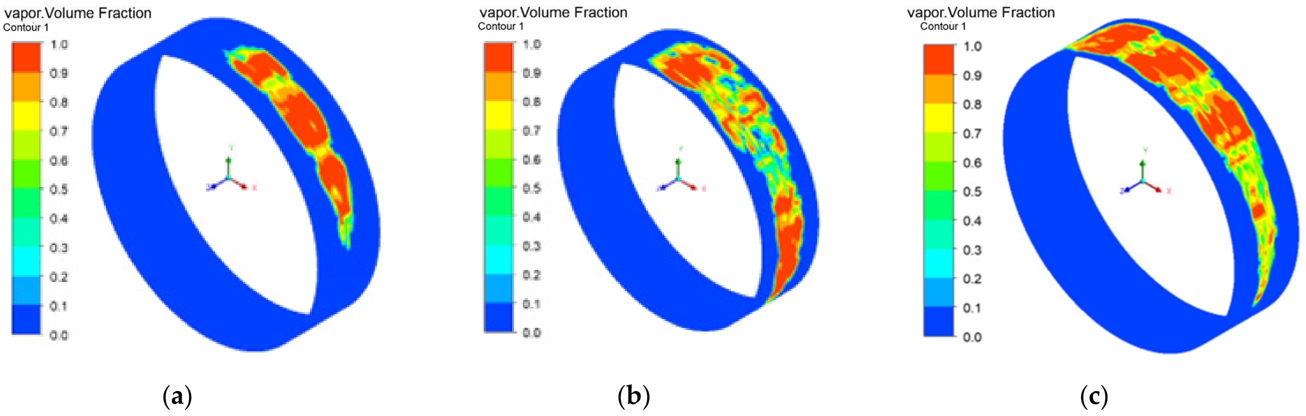

Figure 10. Cavitation when thermal effect is considered: (**a**) $\varepsilon = 0.4, f = 200$ Hz; (**b**) $\varepsilon = 0.4, f = 300$ Hz; (**c**) $\varepsilon = 0.5, f = 200$ Hz.

4.2. An Analysis on the Influence of Thermal Effect on Air Ingestion

Air ingestion is considered a two–phase phenomenon widely existing in open–end SFDs. According to the literature [11], when the eccentricity ratio of open–end SFDs is set as 0.3 and 0.4, with the increase in procession frequency, the relative error between the CFD simulation result and the experimental result is gradually enlarged in terms of oil–film damping. The reason for this is that the thermal effect is ignored by CFD calculations. Therefore, the model in reference [11] considered the thermal effect in numerical simulations to verify the correctness of the numerical simulation.

The SFD structure and boundary conditions of the model provided by the literature [11] are shown in Figure 11, in which the diameter $D = 73.8$ mm, radius clearance $c = 0.14$ mm, axial width $L = 20.6$ mm, supply groove width $Lg = 1.2$ mm, height $h = 0.8$ mm, diameter of inlet $d = 1$ mm, and static eccentricity es = 0.05 mm. The boundary conditions are listed in Table 2. External air is free to go in and out along the opening boundary according to the pressure of the flow field and environment. Through CFX simulation, the oil–film damping of the SFD considering the viscosity thermal effect is calculated, with the eccentricity ratio being 0.3 and 0.4, and the procession frequency being 75–175 Hz. The comparison with the experimental result and the simulation result without considering the viscosity thermal effect is developed. The result of the comparison is shown in Figure 12. When the viscosity thermal effect is considered, the result of numerical simulation is consistent with the experimental result, and the damping error is somewhat reduced. Therefore, it can be proved that heat is generated in the SFD due to squeezing, which affects the damping properties and reduces oil–film damping.

The simulation calculation considering the SFD thermal effect can perform similarly to the actual working condition of the SFD. However, there is a relative error between the calculation result and the experimental result. When the eccentricity ratio is chosen as 0.3 and 0.4 and the procession frequency is set as 75 Hz, the calculated damping result is smaller than the one obtained through the test. However, for other frequencies, the damping value is shown to still be greater than the experimental one. The reason for this may be that the CFD calculation only considers the fluid domain, while the heat transfer in the solid domain is ignored.

Meanwhile, the influence of thermal effect on the volume fraction and range of air ingestion can be discussed and analyzed by the comparison between (a) and (b) of Figures 13–16 under different conditions of eccentricity ratios and procession frequencies. When the thermal effect is considered, the air ingestion phenomenon is more obvious. As shown in Figure 13, with an eccentricity ratio $\varepsilon = 0.3$ and a procession frequency $f = 100$ Hz, it can be observed that the 3D plot of air volume fraction increases significantly under the SFD thermal effect.

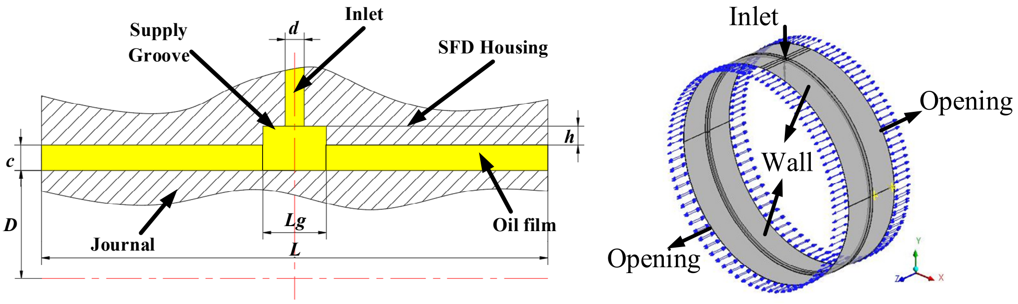

(**a**) (**b**)

Figure 11. (**a**) SFD fluid domain; (**b**) Boundary conditions.

Table 2. SFD Boundary Conditions.

Location	Boundary Condition	Motion State
Axial ends	Opening	Free opening
Supply hole	Inlet	Oil flow = 1 L/min
Outer ring	Wall	Fixed with no slip
Journal	Wall	$X = e \cos(\omega \text{ t})$ $Y = e \sin(\omega \text{ t}) + e_s$

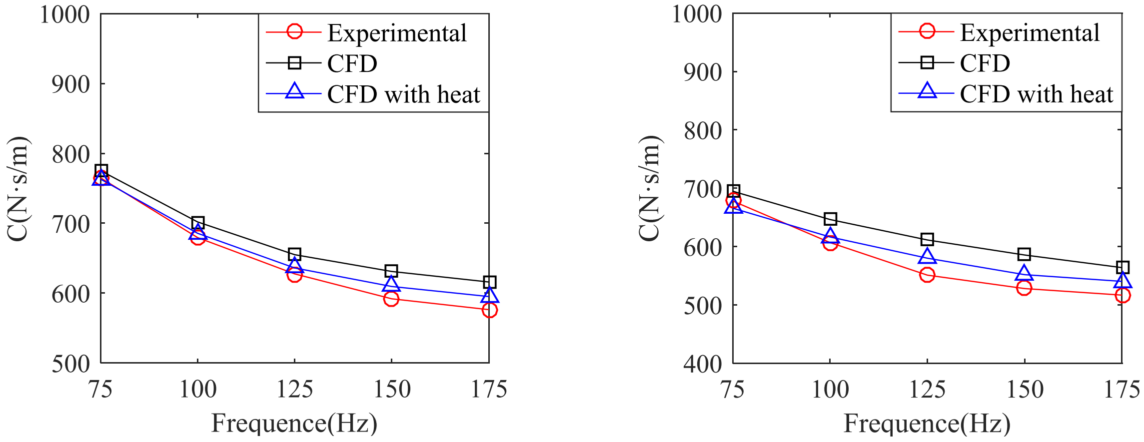

(**a**) (**b**)

Figure 12. Comparison of the damping curves: (**a**) $\varepsilon = 0.3$; (**b**) $\varepsilon = 0.4$.

As shown in the X–axis direction plot, the air ingestion range and volume fraction are both increased. From the Z–axis direction plot of the air ingestion, the zone without air ingestion is weakened slightly, but the air volume fraction on both ends is greatly increased. With an increase in eccentricity ratio and procession frequency, it can be seen in Figure 16 that when eccentricity ratio $\varepsilon = 0.4$ and procession frequency $f = 150$ Hz, the axial air ingestion range and the volume fraction are enhanced significantly. As shown from the Z–axis direction plot of air ingestion, the air ingestion can be seen clearly from the whole circumferential zone of the SFD.

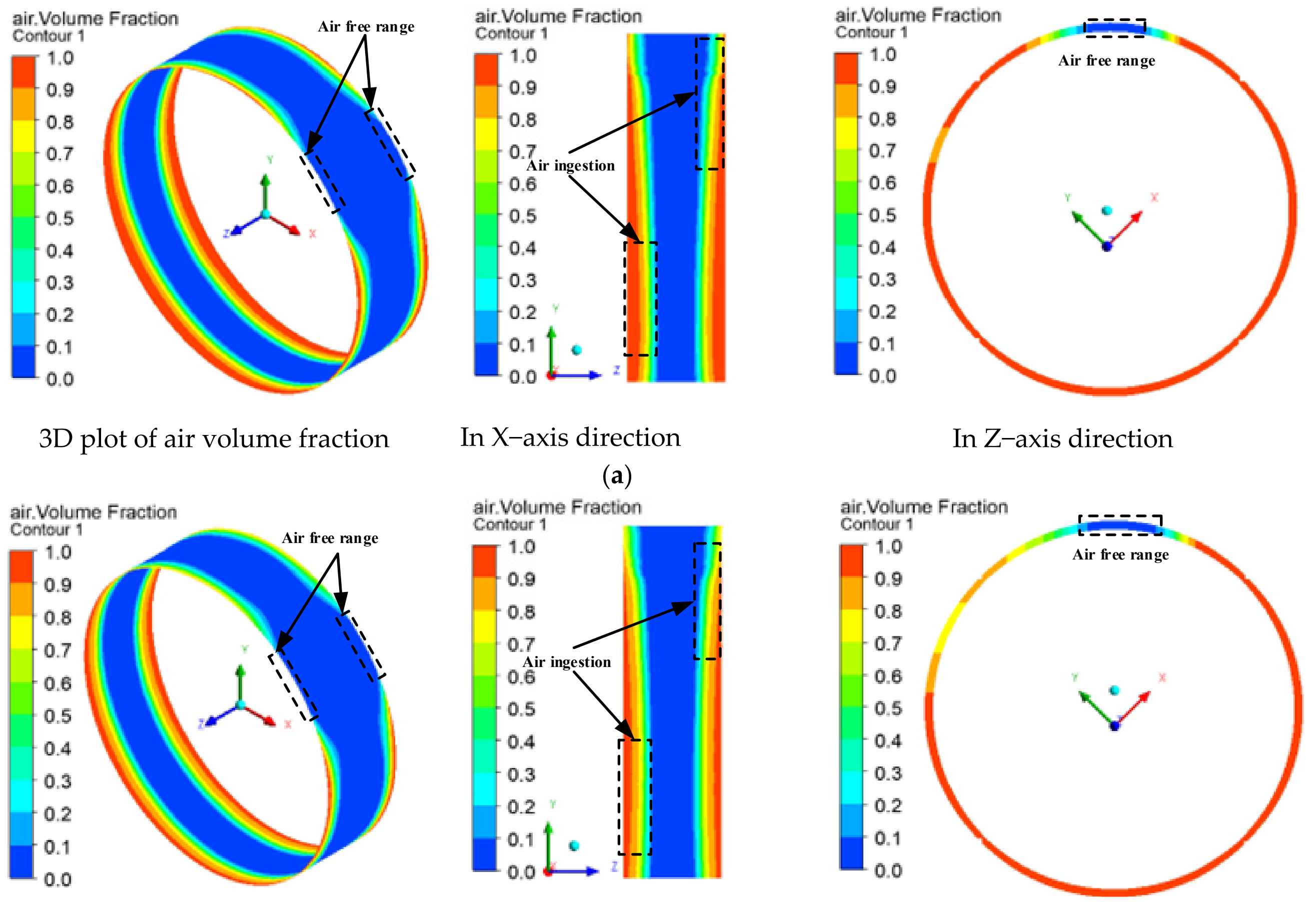

3D plot of air volume fraction In X–axis direction In Z–axis direction

(**a**)

3D plot of air volume fraction In X–axis direction In Z–axis direction

(**b**)

Figure 13. Plot of air volume fraction when ε = 0.3, f = 100Hz: (**a**) The distribution of the air volume fraction with the thermal effect; (**b**) The distribution of the air volume fraction without the thermal effect.

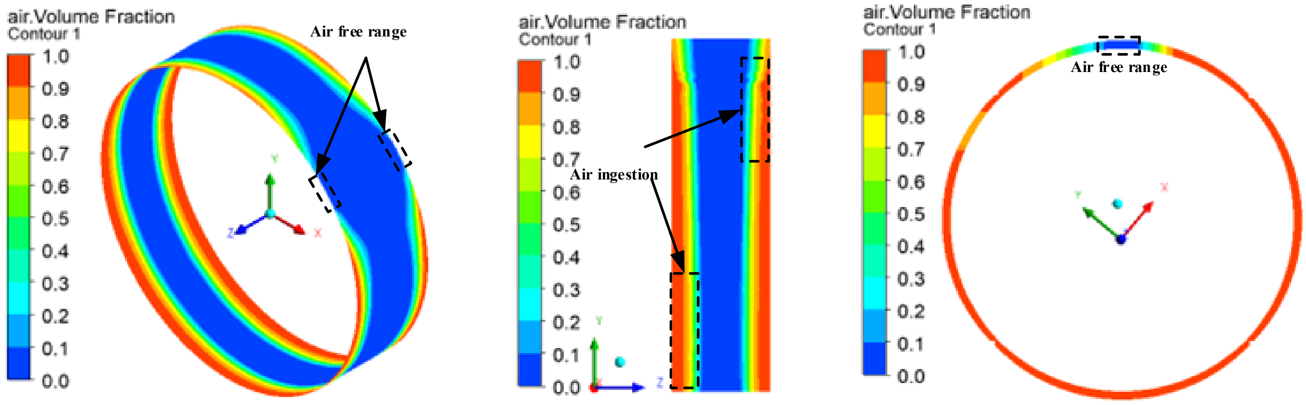

3D plot of air volume fraction In X–axis direction In Z–axis direction

(**a**)

Figure 14. *Cont.*

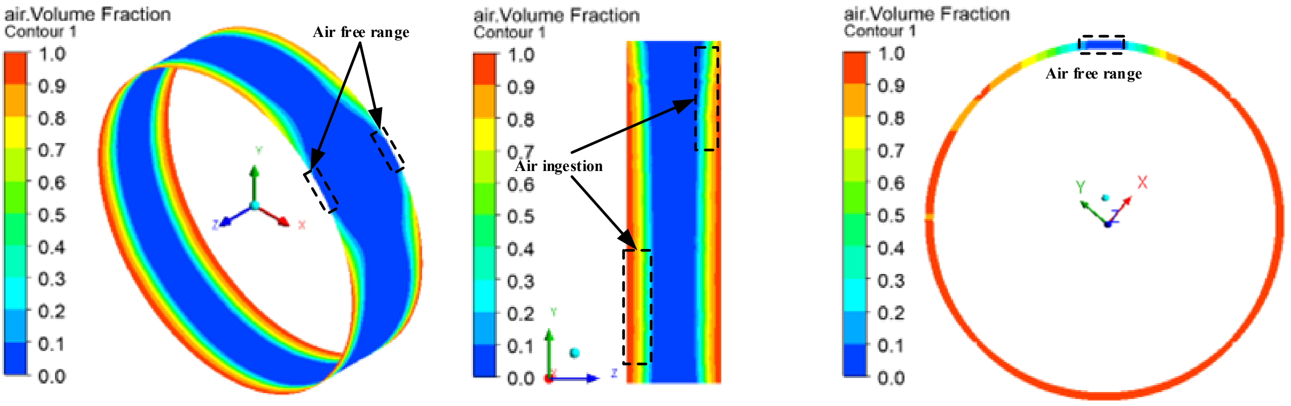

3D plot of air volume fraction In X–axis direction In Z–axis direction

(**b**)

Figure 14. Plot of air volume fraction when ε = 0.3, *f* = 150 Hz: (**a**) The distribution of the air volume fraction with the thermal effect; (**b**) The distribution of the air volume fraction without the thermal effect.

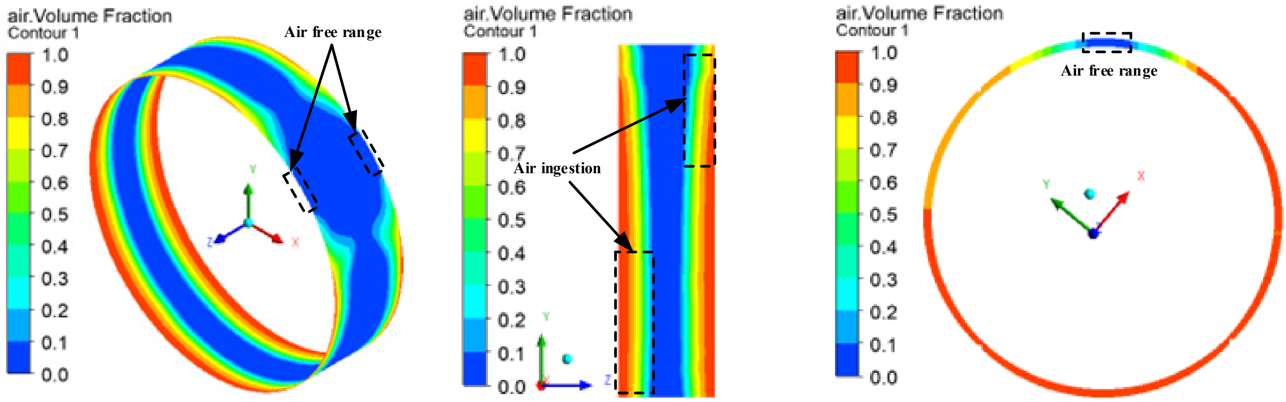

3D plot of air volume fraction In X–axis direction In Z–axis direction

(**a**)

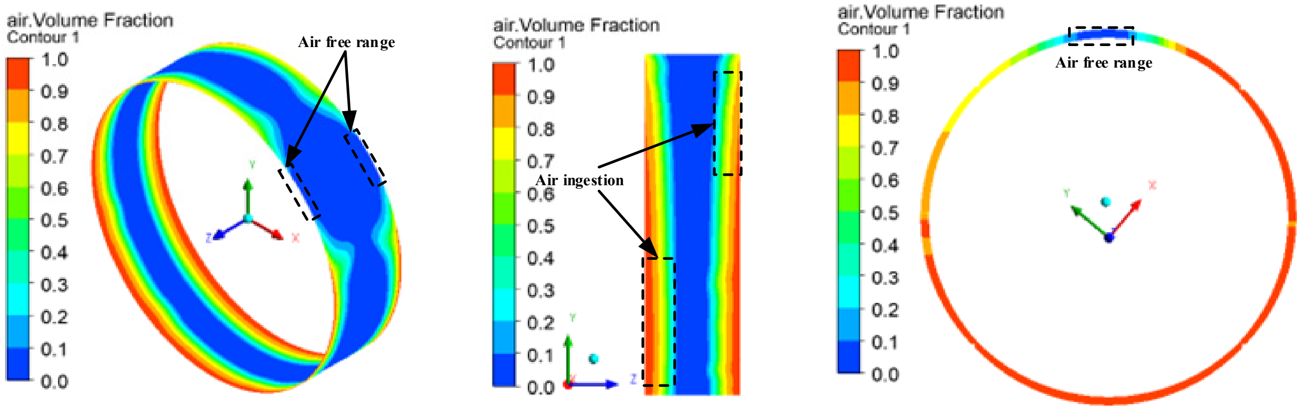

3D plot of air volume fraction In X–axis direction In Z–axis direction

(**b**)

Figure 15. Plot of air volume fraction when ε = 0.4, *f* = 100 Hz: (**a**) The distribution of the air volume fraction with the thermal effect; (**b**) The distribution of the air volume fraction without the thermal effect.

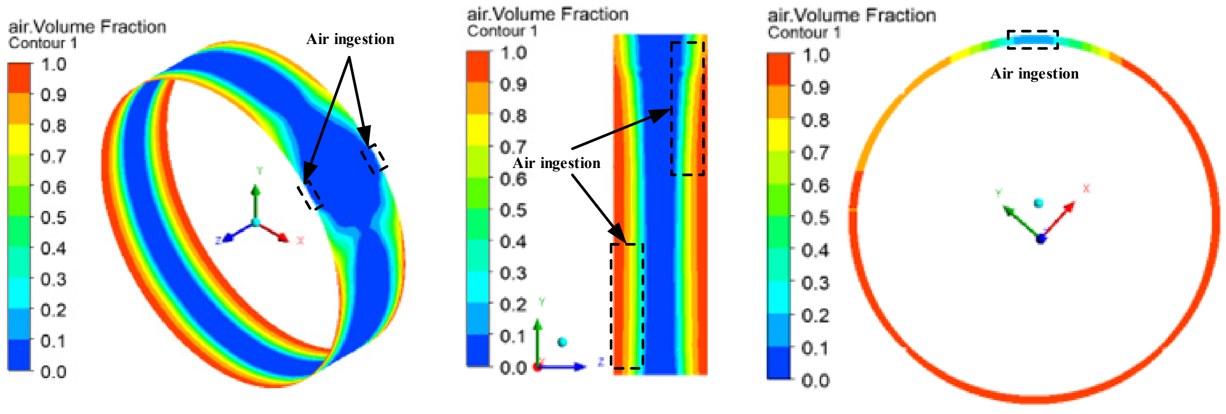

3D plot of air volume fraction In X–axis direction In Z–axis direction

(**a**)

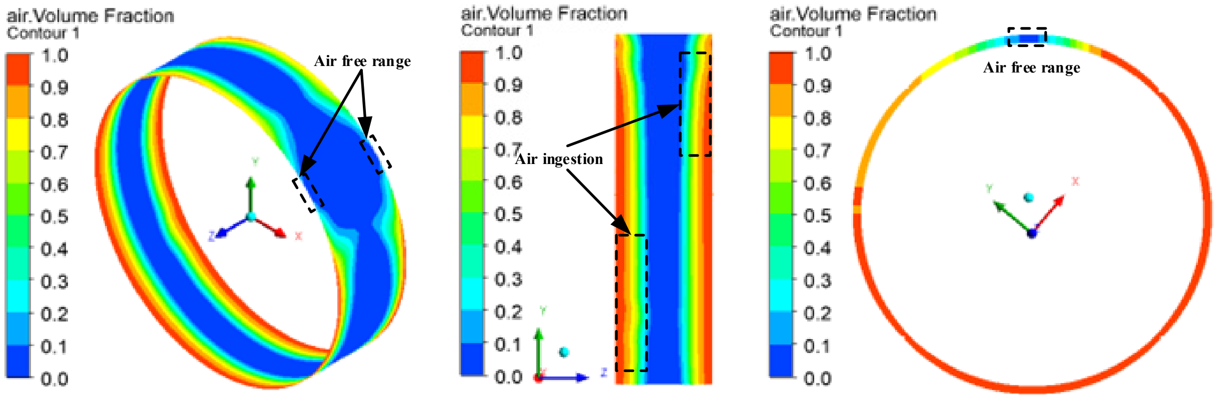

3D plot of air volume fraction In X–axis direction In Z–axis direction

(**b**)

Figure 16. Plot of air volume fraction when $\varepsilon = 0.4$, $f = 150$ Hz: (**a**) The distribution of the air volume fraction with the thermal effect; (**b**) The distribution of the air volume fraction without the thermal effect.

5. Conclusions

In this study, inspired by the oil–film viscosity thermal effect of SFDs, we established a thermohydrodynamic mode and focused on the influence of the oil–film temperature variation and thermal effect on two–phase flow with a variety of operating conditions. With the experimental data of oil–film damping considering two–phase flow, the accuracy of the numerical simulation of thermal effect was verified carefully. The conclusions are as follows:

(1) The maximal temperature of the oil film is gradually enhanced as the procession frequency and the eccentricity ratio increase. With the same reference temperature and an increase in the dynamic viscosity of the oil, the temperature enhancement can be seen apparently. The oil–film temperature field is in symmetrical distribution, whereas the middle part is higher than both ends.

(2) The dynamic viscosity of oil is reduced, caused by the viscosity thermal effect. Compared with oil–film damping at a constant temperature, oil–film damping of the low–viscosity oil decreased by 1.4% at most, whereas it is reduced by 15.9% for the high–viscosity oil. These results make it clear that the temperature–viscosity effect of high–viscosity oil is much more obvious. The damping increases with the increase in the procession frequency; as the temperature of the oil film rises, the effect of this factor weakens.

(3) When the oil–film pressure reaches the saturated vapor pressure, vapor cavitation is formed clearly. The range of the vapor cavitation is enlarged with the increase in procession frequency and eccentricity ratio. According to the SFD thermal effect and based on the law of the conservation of energy, the heat generated by the squeezing oil film is absorbed by the vapor cavitation, thus resulting in strong vaporization and a large amount of vapor cavitations.

(4) Through a comparison with the experimental results in the literature [11], the simulation result of this study is in agreement with the experimental results. In other words, the accuracy of the CFD calculations of the thermal effect was verified practically. This means that the results considering the thermal effect is consistent with that of the experimental conditions. Furthermore, caused by the thermal effect, the air ingestion range and air volume fraction are enlarged considerably, as well as the decrease in the effective squeezing area of the oil film. It is concluded that the thermal effect is related to the air ingested, as well as the oil–film area.

It is concluded that the two–phase flow and the thermal effect of the squeezed oil–film damper considerably affect the dynamic characteristics of the damper. In the present study, the influence performance of two phenomena is developed, and we acknowledge that there is still a lot of work to be carried out and improved in the future.

(1) In this study, the oil–film pressure and the oil temperature are not tested. While increasing the oil–film pressure and the oil temperature, the results may be much better to verify the accuracy of numerical simulation.

(2) The coupling between air ingestion and the vapor cavitation is very complicated, and a lot of works will be explored and discussed for the two–phase flow of the damper under different structure sizes and oil supply conditions.

Author Contributions: Conceptualization, H.Z.; Methodology, H.Z.; Software, G.C. and X.C.; Validation, H.Z. and G.C.; Formal analysis, X.C.; Investigation, X.C. and Y.Z.; Writing—original draft, Y.C.; Writing—review & editing, Y.C.; Project administration, H.Z. All authors have read and agreed to the published version of the manuscript.

Funding: This research was funded by The National Natural Science Foundation of China (grant number 52175106) and Plan for Young and Middle–aged Innovators of Shenyang (grant number RC220326).

Data Availability Statement: The data presented in this study are available on request from corresponding author.

Conflicts of Interest: The authors declare no conflict of interest.

Nomenclature

List of abbreviations	
SFD	Squeeze film damper
List of symbols	
C	Oil−film damping
e	Dynamic eccentric distance
F	Empirical coefficient
F_{cond}	Bubble condensation coefficient
F_t	Tangential force
F_{vap}	Bubble vaporization coefficient
h_{tot}	Total enthalpy
L	Axial length of damper
M_B	Mass of bubble
m_{fg}	Total interphase transfer rate of mass per unit volume
N_B	Number of bubbles per unit volume
p	Oil−film pressure

p_f	Liquid pressure
R_B	Radius of bubbles
R_c	Mass source term of the liquid
R_e	Mass source term of the vapor
R_{nuc}	Bubble radius
r_{nuc}	Volume fraction in bubble core
r_α	Volume fraction of each phase
S_E	Energy source
S_M	Term of generalized momentum source
U_α	Velocity vector of each phase
V_B	Volume of bubble
Γ_α	Mass source in each phase
ρ_α	Density of each phase
ρ_f	Fluid density
ρ_g	Oil vapor density
Ω	Procession rotation speed
θ	Procession angle
σ	Surface tension coefficient

References

1. Koo, B.; San Andrés, L. A Model and Experimental Validation for a Piston Rings–Squeeze Film Damper: A Step Toward Quantifying Air Ingestion. *J. Eng. Gas Turbines Power* **2023**, *145*, 1–13. [CrossRef]
2. Zheng, W.B.; Pei, S.Y.; Zhang, Q.S.; Hong, J. Experimental and theoretical results of the performance of controllable clearance squeeze film damper on reducing the critical amplitude. *Tribol. Int.* **2022**, *166*, 107155. [CrossRef]
3. Feng, N.S.; Hahn, E.J. Density and viscosity models for two–phase homogeneous hydrodynamic damper fluids. *ASLE Trans.* **1986**, *29*, 361–369. [CrossRef]
4. Perreault, M.; Hamzehlouia, S.; Behdinan, K. Application of computational fluid dynamics for thermohydrodynamic analysis of high–speed squeeze–film dampers. *Trans. Can. Soc. Mech. Eng.* **2019**, *43*, 306–321. [CrossRef]
5. Hamzehlouia, S.; Behdinan, K. Thermohydrodynamic modeling of squeeze film dampers in high–speed turbomachinery. SAE International. *J. Fuels Lubr.* **2018**, *11*, 129–146. [CrossRef]
6. San Andrés, L.; Diaz, S.E. Flow visualization and forces from a squeeze film damper operating with natural air entrainment. *J. Tribol.* **2003**, *125*, 325–333. [CrossRef]
7. San Andrés, L.; Barbarie, V.; Bhattacharya, A.; Gjika, K. On the effect of thermal energy transport to the performance of (semi) floating ring bearing systems for automotive turbochargers. *J. Eng. Gas Turbines Power* **2012**, *134*, 1–10. [CrossRef]
8. Yang, Z.; San Andrés, L.; Childs, D. Thermohydrodynamic Analysis of Process–Liquid Hydrostatic Journal Bearings in Turbulent Regime. Part I: The Model and Perturbation Analysis. *J. Appl. Mechamics* **1995**, *63*, 679–684. [CrossRef]
9. Snyder, T.A.; Braun, M.J.; Pierson, K.C. Two–way coupled Reynolds and Rayleigh–Plesset equations for a fully transient, multiphysics cavitation model with pseudo–cavitation. *Tribol. Int.* **2016**, *93*, 429–445. [CrossRef]
10. Tao, L.Y.; Diaz, S.E.; San Andrés, L. Analysis of squeeze film dampers operating with bubbly lubricants. *J. Tribol.* **2000**, *122*, 205–210. [CrossRef]
11. Zhou, H.L.; Chen, X.; Zhang, Y.Q.; Ai, Y.T.; Sun, D. An analysis on the influence of air ingestion on vibration damping properties of squeeze film dampers. *Tribol. Int.* **2020**, *145*, 1–10. [CrossRef]
12. Gehannin, J.; Arghir, M.; Bonneau, O. A volume of fluid method for air ingestion in squeeze film dampers. *Tribol. Trans.* **2016**, *59*, 208–218. [CrossRef]
13. Adiletta, G.; Della Pietra, L. Experimental study of a squeeze film damper with eccentric circular orbits. *J. Tribol.* **2006**, *128*, 365–377. [CrossRef]
14. Bonello, P.; Brennan, M.J.; Holmes, R. A Study of the nonlinear interaction between an eccentric squeeze film damper and an unbalanced flexible rotor. *J. Eng. Gas Turbines Power* **2004**, *126*, 855–866. [CrossRef]
15. Fan, T.S.; Hamzehlouia, S.; Behdinan, K. The effect of lubricant inertia on fluid cavitation for high–speed squeeze film dampers. *J. Vibroeng.* **2017**, *19*, 6122–6134. [CrossRef]
16. San Andrés, L.; De Santiago, O.C. Dynamic response of squeeze film dampers operating with bubbly mixtures. *J. Eng. Gas Turbines Power* **2004**, *126*, 408–415. [CrossRef]
17. San Andrés, L.; Den, S.; Jeung, S.H. On the Force Coefficients of a Flooded, Open Ends Short Length Squeeze Film Damper: From Theory to Practice. *J. Eng. Gas Turbines Powerm* **2018**, *140*, 1–11. [CrossRef]
18. San Andrés, L.; Koo, B. Model and experimental verification of the dynamic forced performance of a tightly sealed squeeze film damper supplied with a bubbly mixture. *J. Eng. Gas Turbines Power* **2020**, *142*, 1–12. [CrossRef]
19. San Andrés, L.; Rodriguez, B. On the Experimental Dynamic Force Performance of a Squeeze Film Damper Supplied Through a Check Valve and Sealed With O–Rings. *J. Eng. Gas Turbines Power* **2021**, *142*, 1–9.

20. Bakir, F.; Rey, R.; Gerber, A.G. Numerical and Experimental Investigations of the Cavitating Behavior of an Inducer. *Int. J. Rotating Mach.* **2004**, *10*, 15–25. [CrossRef]
21. Xing, C.; Braun, M.J.; Li, H.A. Three–Dimensional Navier–Stokes–Based Numerical Model for Squeeze–Film Dampers. Part 1–Effects of Gaseous Cavitation on Pressure Distribution and Damping Coefficients without Consideration of Inertia. *Tribol. Trans.* **2009**, *52*, 680–694. [CrossRef]
22. Miling, N.K. Numerical Simulation of Fluid Field inside a Squeeze Film Damoer and the Study of the Effectof Cavation on the Pressure Distribution. Master's Thesis, Texas A & M University, College Station, TX, USA, 2012.
23. Zwart, P.J.; Gerber, A.G.; Belamri, T. A two–phase flow model for predicting cavitation dynamics. In Proceedings of the Fifth International Conference on Multiphase Flow, Yokohama, Japan, 30 May 2004.
24. Liu, D.M.; Liu, S.H.; Wu, Y.L.; Xu, H.Y. A thermodynamic cavitation model applicable to high temperature flow. *Therm. Sci.* **2011**, *15*, 95–101. [CrossRef]
25. Wang, Y.; Sun, X.; Dai, Y.; Wu, G.; Cao, Y.; Huang, D. Numerical investigation of drag reduction by heat–enhanced cavitation. *Appl. Therm. Eng.* **2015**, *75*, 193–202. [CrossRef]
26. Jang, G.; Chang, D. Analysis of a hydrodynamic herringbone grooved journal bearing considering cavitation. *J. Tribol.* **2000**, *122*, 103–109. [CrossRef]
27. Adiletta, G. An insight into the dynamics of a rigid rotor on two–lobe wave squeeze film damper. *Tribol. Int.* **2017**, *116*, 69–83. [CrossRef]
28. Zhou, H.L.; Chen, X.; Zhang, C.S. Numerical simulation and influence factors analysis for dynamic characteristics of squeeze film damper. *J. Vibroeng.* **2020**, *22*, 1593–1605. [CrossRef]
29. Mojica, L.P.M. Experimental Dynamic Forced Performance of a Centrally Grooved, End Sealed Squeeze Film Damper. Master's Thesis, Texas A & M University, College Station, TX, USA, 2011.